

Cite this: *Energy Environ. Sci.*,
2025, 18, 7635

Three-dimensional bowl-shaped solid additive achieves 20.52% efficiency organic solar cells with enhanced thermal stability *via* curvature-mediated morphology regulation†

Zhicheng Zhong,^{‡a} Sergio Gámez-Valenzuela,^{‡a} Jin-Woo Lee,^b Yufei Wang,^c Bolin Li,^a Guanshui Xie,^{‡d} Weijie Zhou,^a Changjing Xu,^a Dingqin Hu,^{‡a} Haihui Cai,^a Qing Lian,^a Longbin Qiu,^{‡d} Guangye Zhang,^c Mingwei An,^{*ae} Yang Wang,^{‡e} Bumjoon J. Kim,^{‡b} Xugang Guo^{‡*a} and Bin Liu^{‡*a}

High-performance organic solar cells (OSCs) demand precise control over the active layer morphology, as it greatly influences exciton dissociation and charge transport. Solid additives offer a powerful strategy for improved molecular stacking and fine-tuned film morphology. However, most existing additives rely on planar molecular structures, while three-dimensional (3D) fullerene derivatives often suffer from tedious synthesis and poor solubility. Here, we introduced two polycyclic aromatic solid additives, 3D bowl-shaped corannulene and planar coronene with simple structures, into the benchmark PM6:L8-BO system to explore the impact of molecular curvature of additives on OSC performance. The unique curvature of corannulene generates a strong dipole moment, enhancing molecular packing and fostering favorable intermolecular interactions. This, in turn, optimizes nanoscale phase separation, mitigates energy losses, and facilitates efficient charge transfer. As a result, OSCs processed with corannulene achieved an impressive power conversion efficiency of 20.52% and exceptional thermal stability, with an experimentally determined T_{85} lifetime of 2007 h, dramatically surpassing the 52-h lifetime of as-cast devices. These results demonstrate the potential of curved molecular additives in optimizing blend morphology and improving crystallinity, offering new avenues for the development of high-performance and long-lifetime OSCs.

Received 9th April 2025,
Accepted 24th June 2025

DOI: 10.1039/d5ee01977j

rsc.li/ees

Broader context

Organic solar cells (OSCs) represent a transformative technology for sustainable energy solutions, combining flexibility, cost-efficiency, and scalability. However, optimizing active layer morphology to enhance exciton dissociation and charge transport remains a critical hurdle in achieving high-performance and stable OSCs. Traditional solvent additives, while effective, suffer from issues such as toxicity, instability, and variability, limiting their practical application. In this context, solid additives offer a promising alternative, providing more robust and reproducible enhancements to molecular stacking and aggregation. Yet, the potential of three-dimensional (3D) additives, particularly those with curved geometries, has been largely underexplored. Here, we introduce corannulene, a bowl-shaped polycyclic aromatic compound, as a new solid additive that leverages its unique molecular curvature to improve molecular packing and phase separation in the active layer. The curvature of corannulene induces a stronger dipole moment, optimizing nanoscale morphology and charge transport, leading to a record power conversion efficiency (PCE) of 20.52% and superior thermal stability with a T_{85} lifetime of over 2000 h. This work highlights the potential of curvature-driven design principles in solid-state additives, offering a pathway for more efficient, stable, and reproducible organic photovoltaics, pushing the frontier of OSC technology toward commercial viability.

^a Department of Materials Science and Engineering, Southern University of Science and Technology (SUSTech), Shenzhen, Guangdong 518055, P. R. China. E-mail: guoxg@sustech.edu.cn, liub3@sustech.edu.cn

^b Department of Chemical and Biomolecular Engineering, Korea Advanced Institute of Science and Technology (KAIST), Daejeon 34141, Republic of Korea

^c College of New Materials and New Energies, Shenzhen Technology University, Shenzhen, Guangdong 518118, P. R. China

^d Department of Mechanical and Energy Engineering, SUSTech Energy Institute for Carbon Neutrality, Southern University of Science and Technology (SUSTech), Shenzhen, Guangdong 518055, P. R. China

^e Strait Institute of Flexible Electronics (SIFEFuture Technologies), Fujian Key Laboratory of Flexible Electronics, Fujian Normal University and Strait Laboratory of Flexible Electronics (SLoFE), Fuzhou, Fujian 350117, P. R. China. E-mail: ifemwan@fjnu.edu.cn

† Electronic supplementary information (ESI) available. See DOI: <https://doi.org/10.1039/d5ee01977j>

‡ These authors contributed equally to this work.

Introduction

Organic solar cells (OSCs) have emerged as a promising technology in the field of renewable energy due to their cost-effectiveness, semi-transparency, and flexibility.^{1–6} Recent advancements in donor/acceptor materials^{7,8} together with device engineering^{9–18} have enabled OSCs with a bulk heterojunction (BHJ) structure to achieve power conversion efficiencies (PCEs) exceeding 20%. A key factor driving this progress is the precise control of the active layer morphology, which plays a crucial role in improving exciton dissociation and charge transport, ultimately boosting the performance and stability of OSCs.^{19–24} To this end, various methods, including solvent additives,²⁵ thermal annealing,^{26,27} and solvent treatment,^{28,29} have been developed to fine-tune film crystallinity and phase morphology. Among these, halogenated solvent additives, such as 1-chloronaphthalene and 1,8-diiodooctane, utilize their different solubilizing capability for donor and acceptor materials, effectively optimizing the phase separation and blend morphology of active layers.³⁰ However, solvent additives pose inherent limitations, including device performance variability due to the difficulty of precise dosage incorporation, potential environmental and health hazards associated with toxicity, and long-term instability caused by residual additives, affecting overall device performance and consistency.

In this context, solid additives have emerged as a promising solution to overcome these challenges. Unlike solvent additives, the incorporation of solid additives can effectively regulate intermolecular interactions with the donor and/or acceptor, contributing to more favorable molecular stacking and aggregation behavior.^{31–34} More importantly, their reduced sensitivity to dosage variations can significantly enhance device reproducibility. To date, the design and application of solid additives have been mainly focused on molecules with fully or nearly planar structures, such as those based on thiophene, benzene, or pyrazine units.^{35–39} While effective, these planar geometries show limited versatility in fine-tuning molecular interactions and packing. Alternatively, three-dimensional (3D) solid additives with sp^2/sp^3 hybridized atoms or curved structures have been successfully used to provide broader spatial distribution and promote self-assembly in the active layer.⁴⁰ Despite their potential, most reported 3D solid additives rely on fullerene derivatives, which are challenging to synthesize and suffer from poor solubility.⁴¹ Therefore, there is an urgent need to develop new 3D solid additives with simple structures and good solubility to fine-tune OSC morphology and improve device performance.

Corannulene, a bowl-shaped molecule composed of five benzene rings surrounding a central five-membered ring, emerges as a promising candidate for this purpose.^{42–46} The curved geometry of corannulene endows distinct electronic environments on its concave and convex surfaces, offering different electron distributions compared to planar molecules. Additionally, corannulene has a relatively simple molecular structure and excellent solubility compared to more complex fullerene-based solid additives, making it easier to mix with active layer materials to form stable blend films. Moreover, as a non-volatile solid additive, corannulene can

overcome the stability issue associated with the evaporation of liquid additives, ensuring better reproducibility and long-term stability in devices.⁴⁷

Considering these attributes, we herein presented two polycyclic aromatics-based solid additives, the bowl-shaped corannulene and the planar coronene, to systematically investigate how molecular geometry influences the packing of active layer materials, morphology, and the resulting photovoltaic properties in OSCs, aiming at exploring the potential of 3D solid additives. The unique curvature of corannulene results in favorable intermolecular interactions within the donor/acceptor system compared to the planar coronene—sufficient to guide molecular assembly without inducing over-aggregation—thereby facilitating the improved molecular orientation of acceptor materials. This leads to enhanced phase separation, which is essential for efficient charge transport and exciton dissociation. As a result, the OSCs incorporating corannulene achieved a remarkable PCE of 20.52%, surpassing those of devices processed with coronene (14.50% PCE), and marking one of the highest efficiencies reported for OSCs. Furthermore, the devices based on corannulene demonstrated superior thermal stability, with a recorded T_{85} lifetime of 2007 h, starkly contrasting to the as-cast devices (52 h). These findings highlight the considerable promise of corannulene as a solid additive in OSCs, offering a simple yet highly effective approach to optimize BHJ morphology and ultimately improve both efficiency and stability of organic photovoltaics.

Results and discussion

The chemical structures of the polymer donor PM6, the small molecule acceptor L8-BO, and the two solid additives are shown in Fig. 1a. In our study, corannulene was synthesized *via* an eight-step route starting from 2,7-dihydroxynaphthalene, as shown in Fig. S1 (ESI[†]).⁴⁸ The chemical structure of corannulene was confirmed by ¹H NMR spectroscopy (Fig. S2, ESI[†]), showing well-resolved signals consistent with a high-purity product. To gain initial insight into the intrinsic molecular properties of these materials, we performed density functional theory (DFT) calculations on isolated species in the gas phase. Specifically, a monomeric unit of PM6, the L8-BO acceptor, and each additive were optimized at the B3LYP/6-31G** level of theory, where long alkyl side chains were replaced with methyl groups to reduce computational cost. The resulting electrostatic surface potentials (ESPs), depicted in Fig. 1b, reveal that the ESP of L8-BO predominantly showed positive values across most of the isosurface, particularly in the benzothiadiazole-thiophene-pyrrole-benzothiadiazole (BTP) core moiety. In contrast, the central regions of the solid additives with varying configurations displayed notable negative charge densities. According to the antipolar attraction theory, these significant negative charges suggest potential for stronger intermolecular interactions between the L8-BO and solid additives. In addition, the bowl-shaped structure of corannulene, with its concave and convex conformations, features distinct electronic environments, leading to a large dipole moment of 1.77 Debye

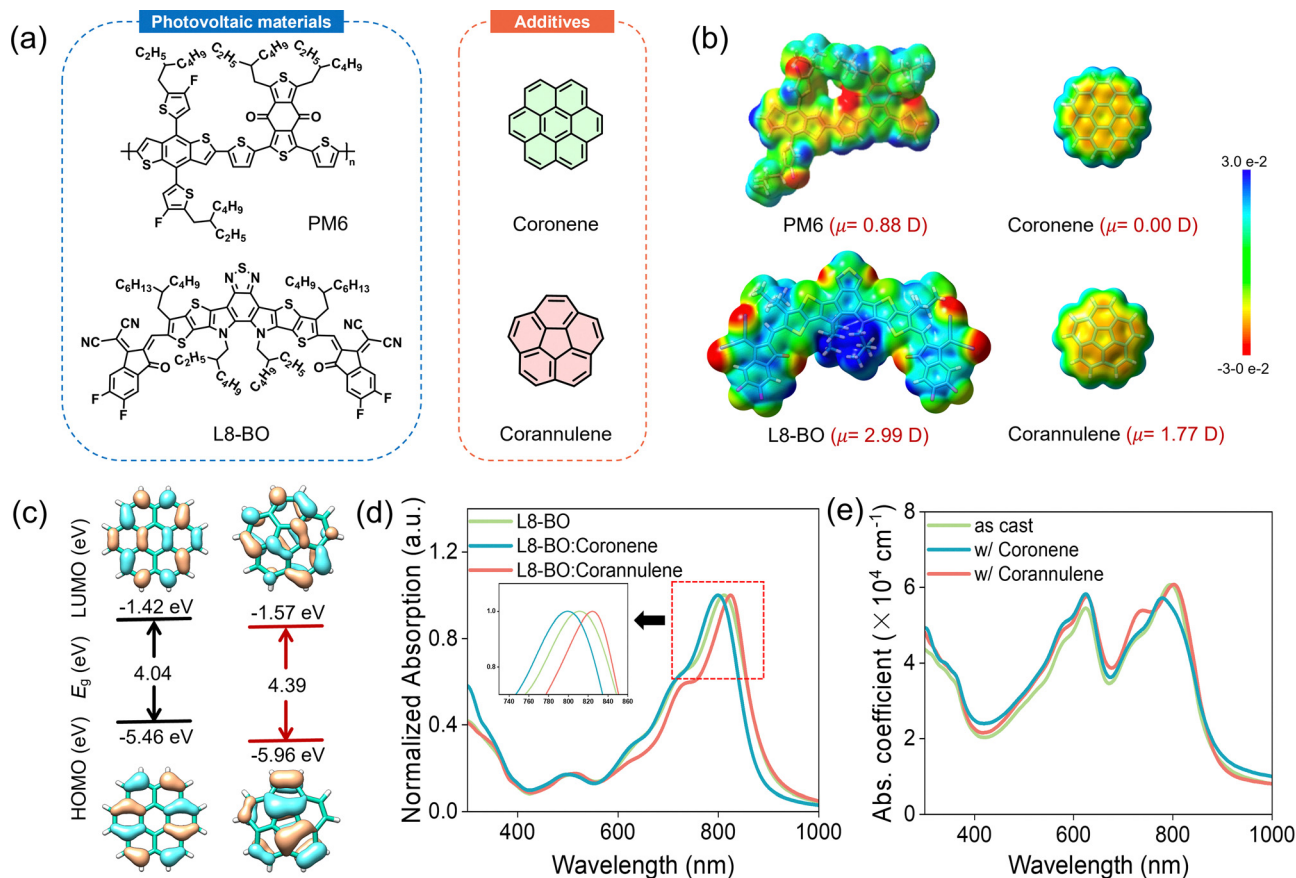


Fig. 1 (a) Chemical structures of PM6, L8-BO, and the solid additives coronene and corannulene. (b) ESP distributions and molecular dipole moments for PM6, L8-BO, coronene and corannulene. (c) Calculated HOMO/LUMO energy levels for coronene and corannulene. (d) Normalized absorption spectra of L8-BO film, and L8-BO films treated with coronene or corannulene. (e) Absorption spectra of PM6:L8-BO, coronene-treated and corannulene-treated blend films.

(D), which is notably higher than that of the flat and centrosymmetric coronene molecule (0 D). The substantial dipole moment of corannulene is believed to drive more pronounced molecular self-assembly, potentially facilitating tighter molecular stacking of the acceptor L8-BO.⁴⁹ As shown in Fig. 1c, the highest occupied molecular orbital (HOMO) and lowest unoccupied molecular orbital (LUMO) energy levels of corannulene and coronene were found to be $-5.96/-1.57$ and $-5.46/-1.42$ eV, respectively.^{50,51} Thermogravimetric analysis (TGA, Fig. S3, ESI †) showed that both aromatic additives were thermally stable, with decomposition temperatures (at 5% weight loss) of 250 and 349 °C, respectively, confirming their non-volatile nature.⁵²

To further confirm the presence of corannulene after annealing, we performed Fourier transform infrared (FT-IR) spectroscopy supported by DFT-calculations (Fig. S4, ESI †). It should be noted that the FT-IR spectra of PM6 and L8-BO systems show numerous bands in the spectral region from 1500 to 1600 cm^{-1} , making it challenging to assign the bands specifically related to corannulene. However, some distinctions can be observed at lower wavenumbers. Notably, corannulene exhibits distinct bands at 545 and 840 cm^{-1} (highlighted in pink), which are absent in the spectrum of the PM6:L8-BO blend. Specifically, the 840 cm^{-1} band corresponds to the out-

of-plane bending vibration mode of C–H, while the band at 545 cm^{-1} arises from out-of-plane ring deformation—a characteristic mode of bowl-shaped polycyclic aromatic hydrocarbons such as corannulene. The persistence of these specific peaks after annealing provides strong evidence for the chemical stability and retention of corannulene in the active layer. Taken together, these results confirm that coronene and corannulene do not volatilize at 65 °C, and the differences observed in device performance cannot be attributed to variations in residual additive content.

The impact of these solid additives on the aggregation properties of PM6 and L8-BO was examined by UV-visible absorption spectroscopy (Fig. 1d and Fig. S5, ESI †).^{53,54} The corannulene-treated L8-BO film exhibited a red-shifted absorption spectrum compared to the L8-BO control film, indicating improved intermolecular interactions and more ordered molecular stacking in thin films. In contrast, the incorporation of coronene disrupted the π - π interaction of L8-BO, leading to a blue-shifted absorption. Notably, the corannulene-treated blend film showed a significantly higher absorption coefficient (6.07×10^4 cm^{-1} , Fig. 1e), suggesting that corannulene can promote optimized molecular packing of active layer components. Both the red-shifted absorption and increased absorption coefficient

should be beneficial to enhancing the short-circuit current (J_{sc}) in OSCs.

To investigate the intermolecular interactions between the aromatic additives and the active layer components, DFT calculations were performed on a series of bimolecular complexes. Each complex consisted of one additive molecule paired with either a PM6 donor fragment modeled as a dimeric unit or a single L8-BO acceptor molecule. A diverse array of energetically favorable conformations was pre-screened and selected for geometry optimization at the B3LYP-D3/6-31G** level of theory. These conformers encompassed a range of interaction sites across distinct moieties of PM6 and L8-BO, and included both concave and convex orientations of the corannulene additive (Fig. 2a–c, Fig. S6, S7 and Table S1, ESI†). It should be noted that although these gas-phase calculations do not account for the full complexity of the condensed-phase morphology, such a first-principle approach based on bimolecular models has proven effective in elucidating critical local interactions relevant to early-stage film formation. In this context, the additives are inclined to interact with the conjugated

backbones of both the donor and acceptor, forming stable complexes *via* π - π or C–H... π interactions with the molecular backbone.⁵⁸ To quantitatively assess the strength of these interactions, interaction energies (E_i) between the additives and PM6 or L8-BO were calculated. Given the bowl-shaped structure of corannulene, the interaction energies were determined for both its concave and convex surfaces with PM6 or L8-BO. The most favorable E_i value between PM6 and coronene was calculated to be -33.79 kcal mol⁻¹, while those for PM6 with corannulene's concave and convex surfaces were estimated to be -26.95 and -26.33 kcal mol⁻¹, respectively (Tables S2 and S3, ESI†). Likewise, for the L8-BO:additive system, a slightly more favorable E_i value of -33.96 kcal mol⁻¹ was obtained for the coronene additive compared to those (-32.21 and -30.49 kcal mol⁻¹) for corannulene's concave and convex surfaces, respectively (Tables S4 and S5, ESI†). Interestingly, these results indicate that the interactions between the additives and the acceptor L8-BO are stronger than those between the additives and PM6. Despite the corannulene's higher molecular dipole moment, its interaction with

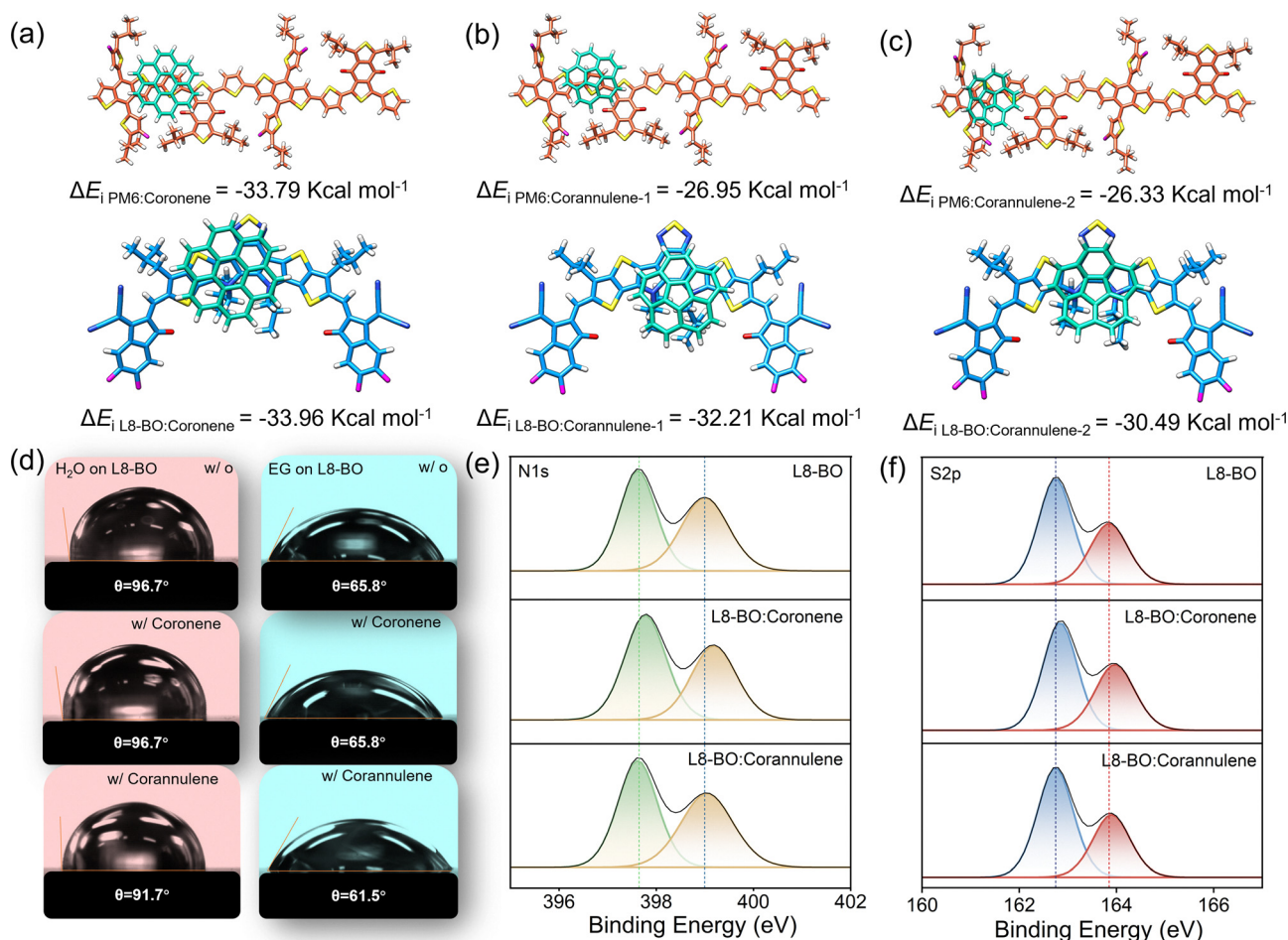


Fig. 2 DFT-optimized geometries and calculated binding energies for the most stable molecular complexes of (a) PM6:coronene, L8-BO:coronene, (b) PM6:corannulene-concave, L8-BO:corannulene-concave, and (c) PM6:corannulene-convex, L8-BO:corannulene-convex. (d) Contact angle images of water and ethylene glycol (EG) droplets on the surfaces of L8-BO, L8-BO:coronene, and L8-BO:corannulene films. (e) O 1s and (f) S 2p XPS spectra of L8-BO, L8-BO:corannulene, and L8-BO:coronene, respectively.

L8-BO was weaker than that of coronene with L8-BO, which arises from the weaker π - π interactions and dominated C-H... π interactions between corannulene and L8-BO molecules.^{58,59} It should be noted that the relatively weaker interaction between corannulene and L8-BO likely prevents excessive aggregation of the acceptor, promoting better molecular packing within the acceptor matrix. This correlates with the observed redshift in the absorption spectra of the L8-BO:corannulene blend compared to the L8-BO:coronene system.

The interaction between solid additives and active layer materials plays a crucial role in determining the miscibility of blend films. This miscibility can be quantitatively characterized by the Flory–Huggins interaction parameter (χ),^{60–63} which is calculated from surface energy measured through contact angle analysis. Compared to the PM6:additive complexes, the incorporation of the corannulene additive with L8-BO resulted in a significantly lower χ value, indicating enhanced miscibility between donor and L8-BO:additive complexes (Table S6, ESI†). Specifically, the addition of corannulene reduced the interaction parameter of L8-BO from 0.021 K to 0.015 K (Fig. 2d and Fig. S8, ESI†), promoting improved blending and favorable interactions at the donor/acceptor (D/A) interface. In contrast, the incorporation of coronene into the L8-BO system led to an increase of 0.109 K in the χ value, adversely affecting the miscibility between the donor and acceptor. This higher χ value suggests that the interaction between coronene and L8-BO is overly strong, potentially leading to excessive acceptor aggregation. It should be noted that evaluating χ parameters using the melting point depression method is not feasible for the PM6:L8-BO system, as PM6 does not exhibit a well-defined melting transition (Fig. S9, ESI†). Additionally, the surface energy method based on contact angle measurements yields only relative rather than absolute values.⁶⁴ X-ray photoelectron spectroscopy (XPS) was employed to further investigate the role of intermolecular interactions.³⁶ As shown in Fig. 2e, f and Fig. S10, S11 (ESI†), no significant changes were observed in the PM6-based systems upon additive incorporation. However, in the L8-BO system doped with coronene, notable shifts in the binding energies of both nitrogen (N) and sulfur (S) elements were detected. Specifically, the binding energy of N shifted from 399.0 eV to 399.2 eV, while that of S increased from 163.8 eV to 164.0 eV. Conversely, negligible variations on the XPS spectra were observed upon the incorporation of corannulene, indicating that corannulene interacts moderately with the acceptor, avoiding excessive aggregation and thereby preserving favorable morphology evolution.

To investigate the impact of the solid additives on OSC performance, conventional devices with a structure of ITO/PEDOT:PSS/active layer/PNDIT-F3N/Ag were fabricated. The meticulous optimization process, detailed in Fig. 3a and Tables S7–S9 (ESI†), included varying the additive concentrations and annealing conditions. The optimal current–voltage (J - V) curves are shown in Fig. 3b, accompanied by the corresponding photovoltaic parameters provided in Table 1. The as-cast device based on the PM6:L8-BO blend without treatment with any additive exhibited an open-circuit voltage (V_{oc}) of 0.877 V, a J_{sc}

of 26.76 mA cm⁻², and a fill factor (FF) of 77.80%, resulting in a PCE of 18.26%. The incorporation of coronene as an additive led to a pronounced decline in performance, with a PCE of 14.50%, V_{oc} of 0.869 V, J_{sc} of 23.24 mA cm⁻², and FF of 71.80%, reflecting a detrimental effect on the device performance. Remarkably, the addition of 15 wt% corannulenes (relative to the donor) into the PM6:L8-BO blend resulted in a notable performance enhancement. The optimized device achieved an increased V_{oc} of 0.897 V, a higher J_{sc} of 28.16 mA cm⁻², and a strengthened FF of 81.24%, ultimately culminating in a PCE of 20.52% (certified efficiency of 19.85%, Fig. S12, ESI†). It should be noted that this efficiency represents one of the highest values ever reported for OSCs to date (Fig. 3c and Table S10, ESI†). Furthermore, the reproducibility for 15 distinct corannulene-treated devices was exceptional, with a PCE distribution narrowly concentrated around 20% (Fig. 3d). Besides, the J_{sc} values integrated from the external quantum efficiency (EQE) spectra (Fig. 3e) of the best-performing devices showed deviations of less than 5% from the ones derived from the J - V characteristics, underscoring the good reliability and consistency of the J - V results.

Ensuring the long-term stability of OSCs remains a major challenge for their commercial viability. Thus, stability was monitored using the maximum power point (MPP) tracking test, in which the stabilized power output (SPO) of OSCs can be evaluated under operational conditions. As illustrated in Fig. 3f, the as-cast device exhibited an SPO value of 18.08% over a duration of 600 s, while the device treated with coronene showed a significant decline to 13.61%. Remarkably, the device modified with corannulene maintained a high SPO value of 19.90% without decay for 600 s, demonstrating superior operational stability. Moreover, the device stability was evaluated under accelerated aging conditions at 65 °C. As depicted in Fig. 3g and Tables S11–S13 (ESI†), the as-cast device manifested a T_{85} lifespan of 52 h, whereas the device incorporating coronene dropped to 85% of its initial efficiency after just 8 h of heating. In stark contrast, the corannulene-treated device demonstrated exceptional stability, with a measured T_{85} lifetime of 2007 h under prolonged heating. This enhanced durability can be attributed to the role of corannulene in promoting more ordered molecular packing within the active layer. By facilitating the formation of well-structured domains, corannulene helps preserve the BHJ morphology over time,^{32,41} preventing the generation of defects or over-aggregation that could compromise the charge transport channels within the blend matrix. This underscores the role of corannulene in improving the long-term stability of OSCs.^{3,58}

The charge carrier dynamics within the devices were systematically investigated to examine the impact of additives on charge transport properties.⁶⁵ The space-charge-limited current (SCLC) measured at least five independently prepared hole-only and electron-only devices at each condition, as presented in Fig. 4a, Fig. S13 and Table S14 (ESI†), revealed the hole/electron mobilities for the as-cast, the coronene-treated, and corannulene-treated devices, which were found to be $3.56 \times 10^{-4}/4.32 \times 10^{-4}$, $1.36 \times 10^{-4}/2.54 \times 10^{-4}$, and $5.22 \times 10^{-4}/5.72 \times 10^{-4}$ cm² V⁻¹ s⁻¹, respectively. The highest and most

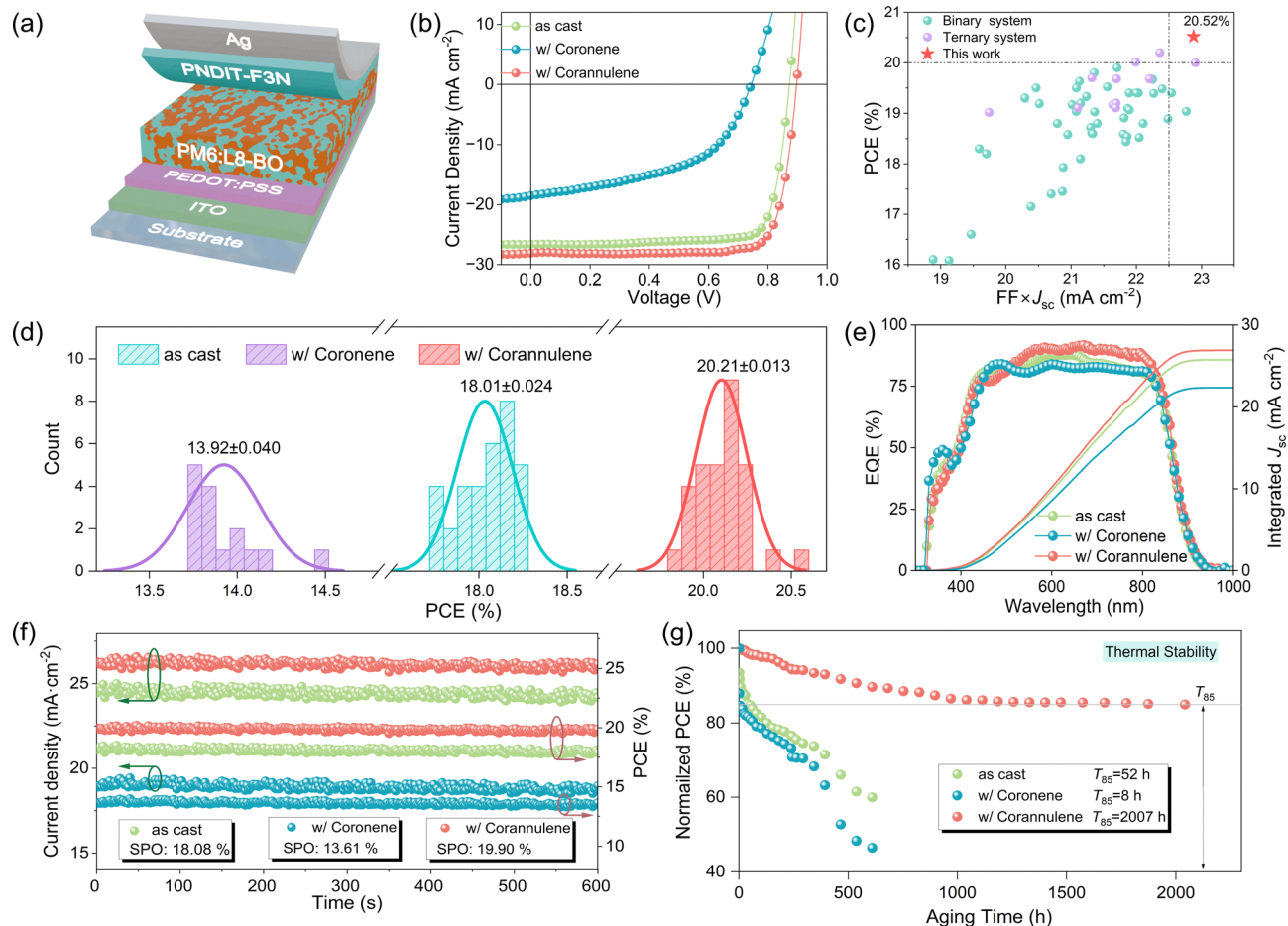


Fig. 3 (a) Schematic illustration of the device architecture for the OSCs used in this work. (b) J - V characteristics of the PM6:L8-BO-based OSCs processed without or with solid additives. (c) Plots of the PCE as a function of $J_{sc} \times FF$ for solid additive-processed binary and ternary OSCs reported over the preceding years. (d) Statistical analysis of the performance of 15 distinct devices based on PM6:L8-BO processed without or with additives. (e) EQE spectra for OSCs together with integrated J_{sc} curves for devices processed without or with distinct additives. (f) Evolution of PCE and J_{sc} for PM6:L8-BO-based OSCs treated without or with solid additives under MPP tracking over time. (g) Thermal stability showing PCE evolution of the as-cast, coronene-treated, and corannulene-treated OSCs.

balanced mobilities observed in the corannulene-modified device resulted in the largest FF and J_{sc} among all the cells. To further evaluate the influence of coronene and corannulene additives on exciton dissociation, the photocurrent density (J_{ph}) and effective voltage (V_{eff}) correlations were then analyzed (Fig. 4b).^{24,66} The corannulene-incorporated device demonstrated an impressive exciton dissociation probability (P_{diss}) of 99.6%, notably higher than that (96.6%) observed in the as-cast device and that (94.9%) in the coronene-doped cell. Additionally, the device incorporating corannulene achieved a superior charge collection efficiency (P_{coll}) of 94.5%, surpassing the as-cast (81.5%) and coronene-based device (72.3%, Table S15, ESI†). The P_{diss} and P_{coll} underscore the substantial enhancement in both exciton dissociation and charge collection efficiency with the inclusion of corannulene. The charge recombination mechanism in OSCs was further explored by analyzing the variation of the J_{sc} with light intensity (P_{light}). The relationship between J_{sc} and P_{light} follows a power law: $J_{sc} \propto P_{light}^\alpha$, where an α value closer to 1 indicates suppressed bimolecular recombination. As illustrated in Fig. 4c, the α values

were 0.90, 0.78, and 0.97 for the as-cast device, the device treated with coronene and corannulene, respectively. Additionally, trap-assisted recombination was assessed by conducting the V_{oc} as a function of P_{light} . The corannulene-processed device exhibited a slope closer to 1 compared to the as-cast and coronene-treated devices (Fig. S14, ESI†), demonstrating effective suppression of trap-assisted recombination with the corannulene modification.

Further insights into the effects of the coronene and corannulene additives on charge extraction and recombination were obtained through characterizations of transient photoconductivity (TPC) and transient photovoltage (TPV), as illustrated in Fig. 4d and e.^{67,68} The device treated with corannulene yielded a faster charge extraction time (τ_1) of 0.153 μ s and a longer carrier lifetime (τ_2) of 2.221 μ s compared to the coronene-regulated (τ_1 : 0.217 μ s; τ_2 : 0.519 μ s) and the as-cast (τ_1 : 0.202 μ s; τ_2 : 1.502 μ s) OSCs. The accelerated charge extraction process in the corannulene-processed device facilitates more efficient charge collection and helps suppress recombination losses. Simultaneously, the prolonged carrier

Table 1 Photovoltaic performance parameters of OSCs based on PM6:L8-BO system treated with various solid additives

Active layer ^a	V_{oc} (V) ^c	J_{sc} (mA cm ⁻²) ^c	Cal. J_{sc} ^b (mA cm ⁻²)	FF (%) ^c	PCE (%) ^c
As cast	0.877 (0.876 ± 0.003)	26.76 (26.57 ± 0.569)	25.28	77.80 (77.34 ± 0.662)	18.26 (18.01 ± 0.024)
w/Coronene (10%)	0.869 (0.864 ± 0.003)	23.24 (22.76 ± 0.239)	22.32	71.80 (70.58 ± 0.989)	14.50 (13.92 ± 0.040)
w/Corannulene (15%)	0.897 (0.891 ± 0.005)	28.16 (27.95 ± 0.214)	26.89	81.24 (80.80 ± 0.646)	20.52 (20.21 ± 0.013)
w/Corannulene (15%) ^d	0.899	27.98	—	78.90	19.85

^a Device area is 6.4 mm² with the use of a shadow mask. ^b J_{sc} integrated from the EQE curves. ^c Average values with standard deviation from 15 devices included in parenthesis. ^d Certified results from South China National Center of Metrology.

lifetime contributes to lower non-radiative voltage losses, ultimately leading to a higher V_{oc} .⁶⁹ Furthermore, time-resolved photoluminescence (TRPL) measurements were conducted to study the exciton dissociation kinetics.⁷⁰ As detailed in Fig. S15 and Table S16 (ESI[†]), the TRPL decay curves, probed at 560 nm, were fitted by a bi-exponential lifetime model. The average decay lifetimes were determined to be 0.257, 0.250, and 0.256 ns for the films treated with corannulene, coronene, and the as-cast, respectively. The longer nonradiative lifetime observed in the corannulene-modified film manifested reduced charge recombination. In addition, an excitation wavelength of 560 nm was employed to selectively excite the donor in the photoluminescence (PL) quenching experiments while minimizing absorption by the acceptor L8-BO. This approach ensures that the observed quenching originates primarily from donor exciton dissociation without contributions from acceptor-related processes (Fig. S16, ESI[†]). The corannulene-processed film demonstrated a higher PL quenching efficiency (98.8%) compared to both the coronene-treated (81.7%) and as-cast analogs (78.8%, Fig. 4f). This finding indicates enhanced charge transfer between PM6 and L8-BO in the corannulene-

treated film, confirming that corannulene boosts more efficient exciton dissociation and charge transport in OSCs.

Femtosecond transient absorption spectroscopy (fs-TAS) was conducted to explore the dynamics of photo-induced charge transfer in OSCs.^{12,71} A pump wavelength of 810 nm was selected to excite the acceptor, aligning with its characteristic absorption peak. The 2D color plots depicting the transient absorption (TA) images for the blend films are presented in Fig. 5a–c, while the corresponding kinetic curves at 580 nm and 810 nm are displayed in Fig. 5d–f. The ground state bleaching (GSB) signals of the donor and acceptor emerged in the 500–650 nm and 620–850 nm regions, respectively. Upon selectively exciting the acceptor, we monitored a rapid decay of GSB signal at 810 nm, accompanied by a rise in the GSB signal at 580 nm, indicating efficient photoinduced hole transfer from L8-BO to the donor. Compared to the as-cast (0.265 ps), the device treated with corannulene exhibited a shorter exciton lifetime (0.254 ps), indicating enhanced exciton dissociation efficiency. In contrast, the coronene-treated device showed an increased exciton lifetime (0.282 ps), suggesting less efficient dissociation. Regarding charge carrier dynamics, longer charge

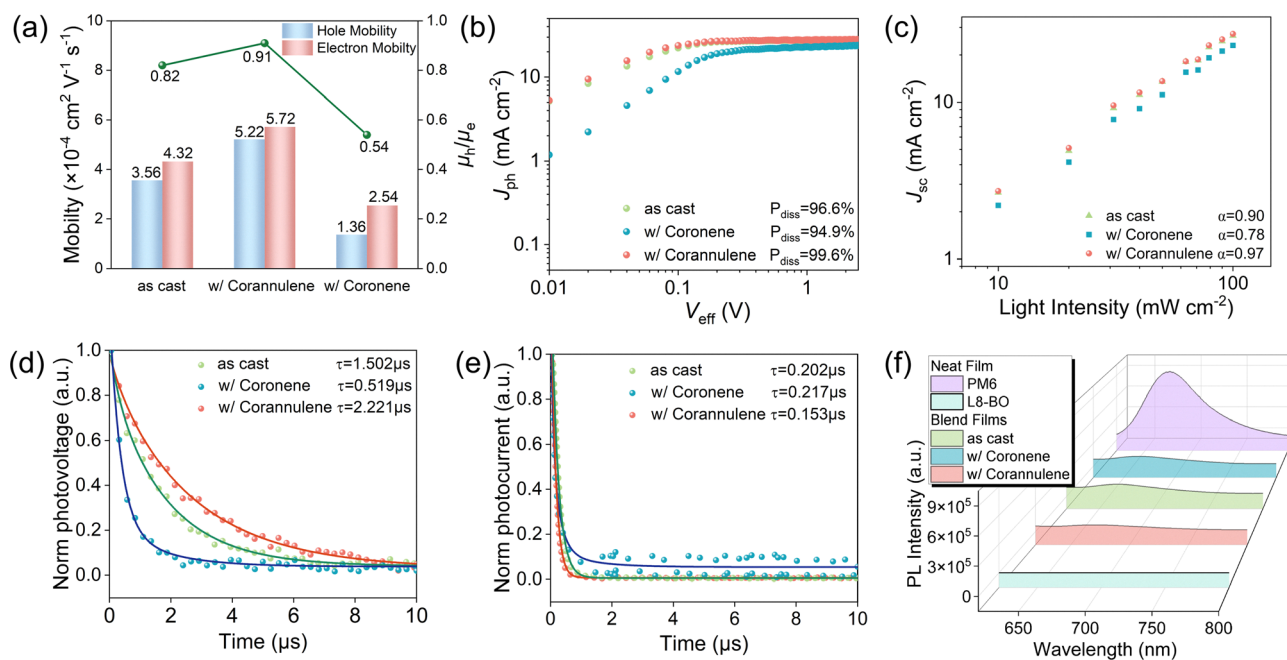


Fig. 4 (a) Hole and electron mobilities and their ratios in PM6:L8-BO-based OSCs processed without or with solid additives. (b) J_{ph} – V_{eff} curves. (c) Dependence of J_{sc} on P_{light} of OSCs. (d) TPV and (e) TPC curves for the corresponding devices. (f) PL spectra of the neat PM6, L8-BO, and blend films.

lifetimes are generally favorable for improving the charge collection. The measured charge lifetimes were 5.5 ns (as-cast), 3.5 ns (coronene-treated), and 6.3 ns (corannulene-treated), respectively, implying that corannulene-treated devices exhibit superior charge collection capabilities compared to as-cast and coronene-treated devices.⁷² The decay dynamics were fitted using the bi-exponential decay model: $I = A_1 \exp(-t/\tau_1) + A_2 \exp(-t/\tau_2)$, where τ_1 corresponds to the exciton dissociation time at the D/A interface, and τ_2 represents the exciton diffusion time within the domains.⁶⁸ The τ_1 and τ_2 values for the corannulene-treated film were found to be 0.60 and 3.29 ps (Fig. S17, ESI†), respectively, shorter than those for the control blend ($\tau_1 = 0.83$ ps and $\tau_2 = 5.88$ ps) and the coronene-doped film ($\tau_1 = 1.29$ ps and $\tau_2 = 6.73$ ps). These shorter times suggest faster exciton dissociation and diffusion in the corannulene-modified film, leading to suppressed exciton recombination while yielding enhanced J_{sc} and FF.

To better understand the significant improvement in V_{oc} observed in the corannulene-treated devices, we examined the corresponding energy losses.^{73,74} According to the Shockley–Queisser (SQ) limit and equilibrium theory, the total energy losses can be categorized into three components: ΔE_1 (radiative recombination loss above the bandgap), ΔE_2 (radiative

recombination loss below the bandgap), and ΔE_3 (non-radiative recombination loss).⁷⁵ ΔE_1 can be calculated using the formula $E_g - V_{oc}^{SQ}$, where E_g is the bandgap of the blend films, and V_{oc}^{SQ} is the theoretical maximum V_{oc} as predicted by the SQ model. Thus, ΔE_1 (0.263 eV) arises directly from the fundamental bandgap and represents an intrinsic limitation. As depicted in Fig. 5g and h, the E_2 values were determined using the Fourier-transform photocurrent spectroscopy (FTPS) and electroluminescence (EL) spectra. The subtle differences in ΔE_2 were noted among the devices, with the corannulene-modified device showing a reduced value of 0.055 eV compared to the as-cast (0.058 eV). Additionally, incorporating corannulene as the solid additive into the PM6:L8-BO system led to a decrease in ΔE_3 from 0.248 eV to 0.233 eV. The detailed energy loss analysis in Fig. 5i further illustrates that the PM6:L8-BO-based OSCs incorporating corannulene exhibit a reduction in the total ΔE value from 0.569 eV to 0.551 eV, thereby lowering energy losses and resulting in an enhanced V_{oc} .

Atomic force microscopy (AFM) and transmission electron microscopy (TEM) were carried out to further explore the variation of blend film morphologies assisted by the solid additives. As shown in Fig. 6a and Fig. S18 (ESI†), the addition of corannulene to the blend film, which initially had a root-

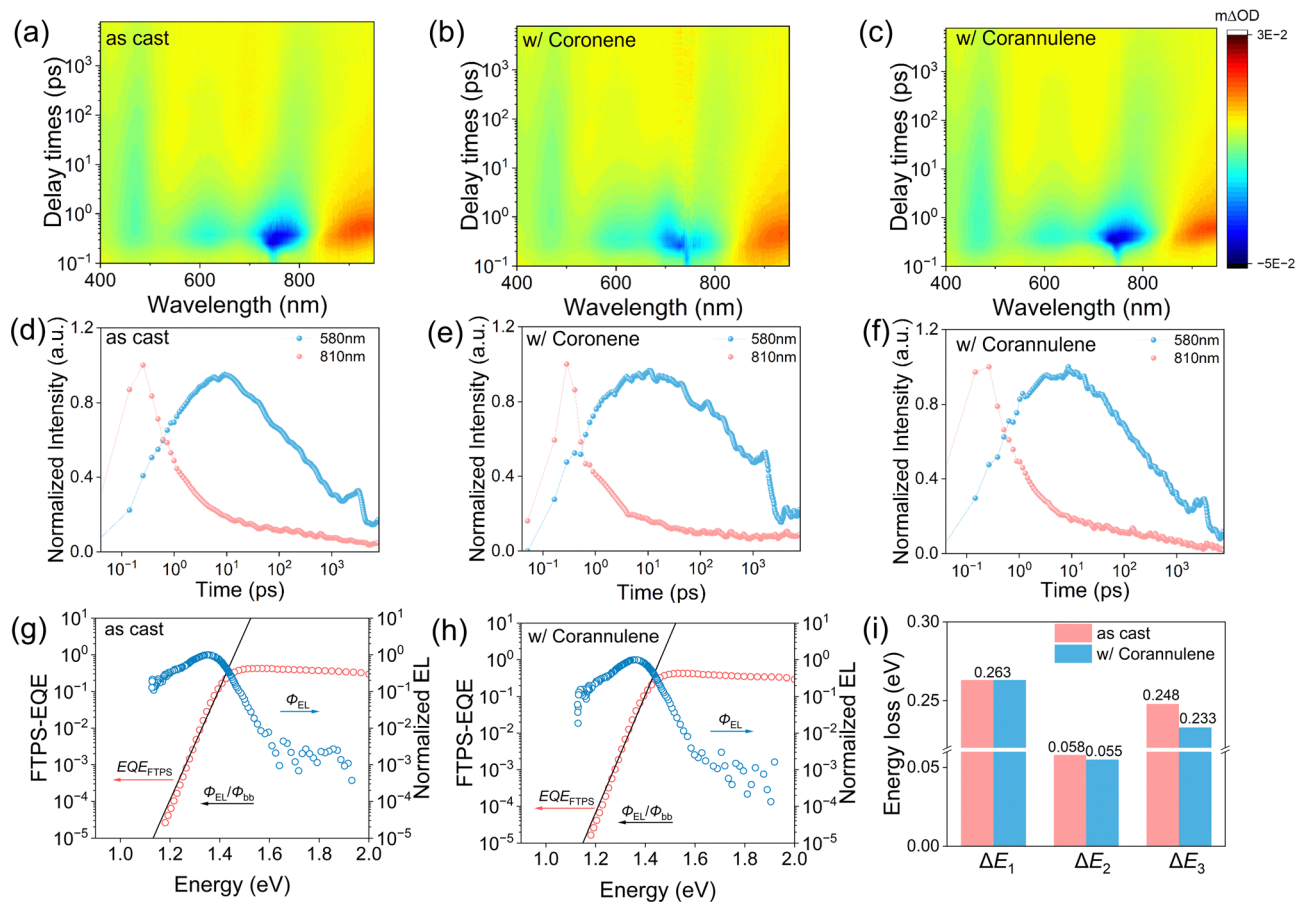


Fig. 5 TAS spectra of PM6:L8-BO binary blends without and with solid additives: (a)–(c) 2D color plots of TAS spectra. (d)–(f) Decay dynamics probed at different wavelengths. FTPS-EQE and EL spectra of the OSCs based on the (g) as-cast and (h) corannulene-treated blend films. (i) Detailed E_{loss} values for the as-cast and corannulene-treated OSCs.

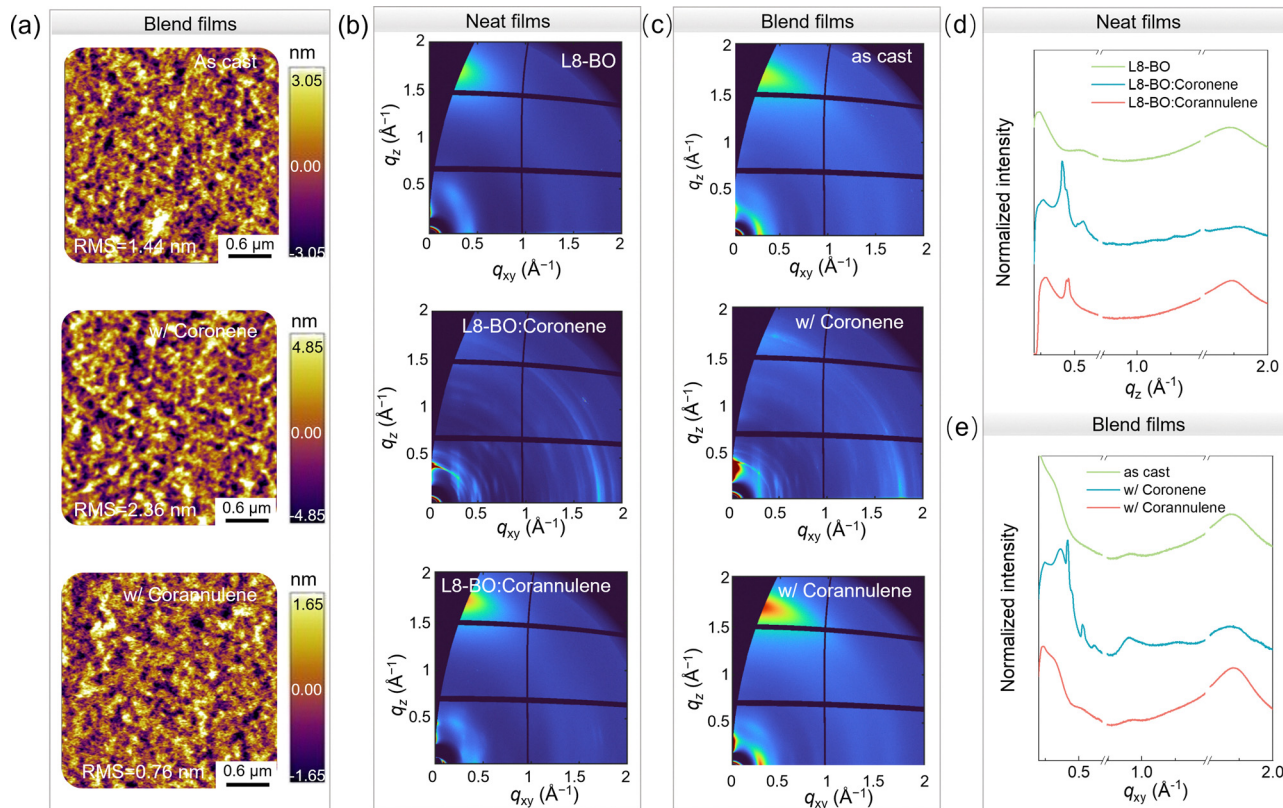


Fig. 6 (a) AFM height images of the as-cast, coronene-treated, and corannulene-treated blend films. (b) 2D-GIWAXS patterns of the neat L8-BO film, coronene-treated and corannulene-treated L8-BO films. (c) 2D-GIWAXS patterns of the corresponding blend films. 2D-GIWAXS line-cut profiles in the (d) OOP and (e) IP directions for the neat L8-BO and corresponding blend films.

mean-square (RMS) roughness of 1.44 nm, resulted in a refined network structure with a reduced RMS roughness value of 0.76 nm. This finding further indicates an enhanced compatibility between the donor and acceptor materials, aligning with the outcomes derived from contact angle measurements. This modification yields a more uniform surface morphology, which in turn minimizes charge trapping, thereby enhancing the overall charge transport within the devices.^{76,77} In contrast, the coronene-treated film displayed a significantly larger RMS of 2.36 nm, indicative of excessive phase separation. Additionally, corannulene-treated PM6:L8-BO films exhibit excellent thermal robustness, as evidenced by AFM height images and stable photovoltaic performance (fluctuating around 20%) across various annealing temperatures (Fig. S19 and Table S8, ESI[†]). TEM analysis further revealed that corannulene-modified blend films exhibit a finely tuned nanoscale morphology (Fig. S20, ESI[†]), facilitating charge transfer while curbing bimolecular recombination.

To elucidate the impact of bowl-shaped corannulene additive on molecular crystallinity and packing properties, grazing-incidence wide-angle X-ray scattering (GIWAXS) was conducted. The GIWAXS patterns and corresponding line profiles along both the out-of-plane (OOP) and in-plane (IP) directions for neat and blend films are presented in Fig. 6b–e, with the crystal coherence length (CCL) values summarized in Tables S17 and S18 (ESI[†]).^{78,79} Given that these two solid additives interact more strongly with the acceptor than with the polymer donor,

we first focused the GIWAXS analysis on L8-BO films. In the OOP direction, the corannulene-treated L8-BO film exhibited a pronounced (010) π - π diffraction peak at $q_z \approx 1.70 \text{ \AA}^{-1}$, slightly upshifted from $q_z \approx 1.69 \text{ \AA}^{-1}$ in the pristine L8-BO film, corresponding to d -spacing values of 3.67 Å and 3.65 Å, respectively. This shift indicates that the incorporation of corannulene effectively promotes face-on molecular orientation, a critical feature for efficient electron transport. In contrast, the coronene-treated L8-BO film displayed an extremely weak (010) diffraction peak at $q_z \approx 1.68 \text{ \AA}^{-1}$ with a shorter d -spacing of 3.56 Å. The stronger interaction between coronene and L8-BO disrupts intermolecular π - π stacking, weakening crystallinity, which can be corroborated by DFT calculations. Furthermore, corannulene significantly enhances molecular stacking and film crystallinity, as reflected by an increase in crystalline coherence length (CCL) from 2.56 nm in pristine L8-BO to 3.40 nm in the corannulene-modified film. On the contrary, the coronene-treated film displayed a notably reduced CCL of 1.87 nm, indicative of diminished crystallinity and a more disordered molecular arrangement of L8-BO.

Upon blending with the PM6:L8-BO system, corannulene-treated films retained their preferential face-on orientation and high crystallinity, evidenced by a significant enhancement in the (010) OOP peak. Moreover, the corresponding CCL value increased from 3.34 nm in the pristine blend to 3.72 nm, indicating substantial improvement in molecular realignment. This enhanced CCL is advantageous for vertical charge transfer

within the blend film, aligning well with the mobility values obtained from the SCLC method. Additionally, integrating corannulene led to a reduced (010) d -spacing from 3.72 \AA^{-1} to 3.70 \AA^{-1} in the OOP direction, further signifying a more compact and crystalline active layer. In contrast, the planar coronene additive exhibited a markedly weaker (010) π - π diffraction peak in the OOP direction, accompanied by a pronounced (100) lamellar stacking peak at $q_{xy} \approx 0.42 \text{ \AA}^{-1}$ in the IP direction. This suggests that coronene with a larger contact surface induces excessive phase separation due to its strong interaction with L8-BO, disrupting face-on orientation and significantly reducing crystallinity.⁵⁸ As a result, coronene incorporation leads to morphological instability and hindered charge transport, ultimately deteriorating device efficiency. These findings highlight the crucial role of corannulene in optimizing molecular ordering and improving photovoltaic performance.

In situ UV-vis absorption spectroscopy was employed to further elucidate the effect of solid additives on the dynamic aggregation behavior of PM6 and L8-BO during the spin-coating process (Fig. 7a-f).^{80,81} The film evolution can be

categorized into four distinct stages, marked by progressive variations in UV-vis absorption, represented by pink, yellow, aquamarine, and blue regions. In the initial stage, the intensity of 0-0 absorption peaks of both donor and acceptor experienced a notable reduction, primarily driven by the rapid solvent evaporation. This was followed by a gradual decline of absorbance in the orange region, indicative of further film thinning under the centrifugal force of spin-coating. A critical transformation occurred in Stage III, where the acceptor underwent a pronounced spectral shift alongside a rapid change in the 0-0 peak intensity. This transition from a liquid-like state to a solid-phase aggregation signifies a structural reorganization, leading to enhanced molecular ordering. Ultimately, the absorption profile of the donor and acceptor stabilized in Stage IV, signifying the completion of film formation. A comparative analysis of the spin-coating dynamics revealed that the corannulene-treated L8-BO films exhibited an extended Stage I (15 ms), indicating prolonged solvent evaporation process, thereby facilitating molecular diffusion and phase separation. Additionally, corannulene treatment accelerated pre-aggregation and aggregation process compared to the as-cast (15 ms), which led to a shortened Stage

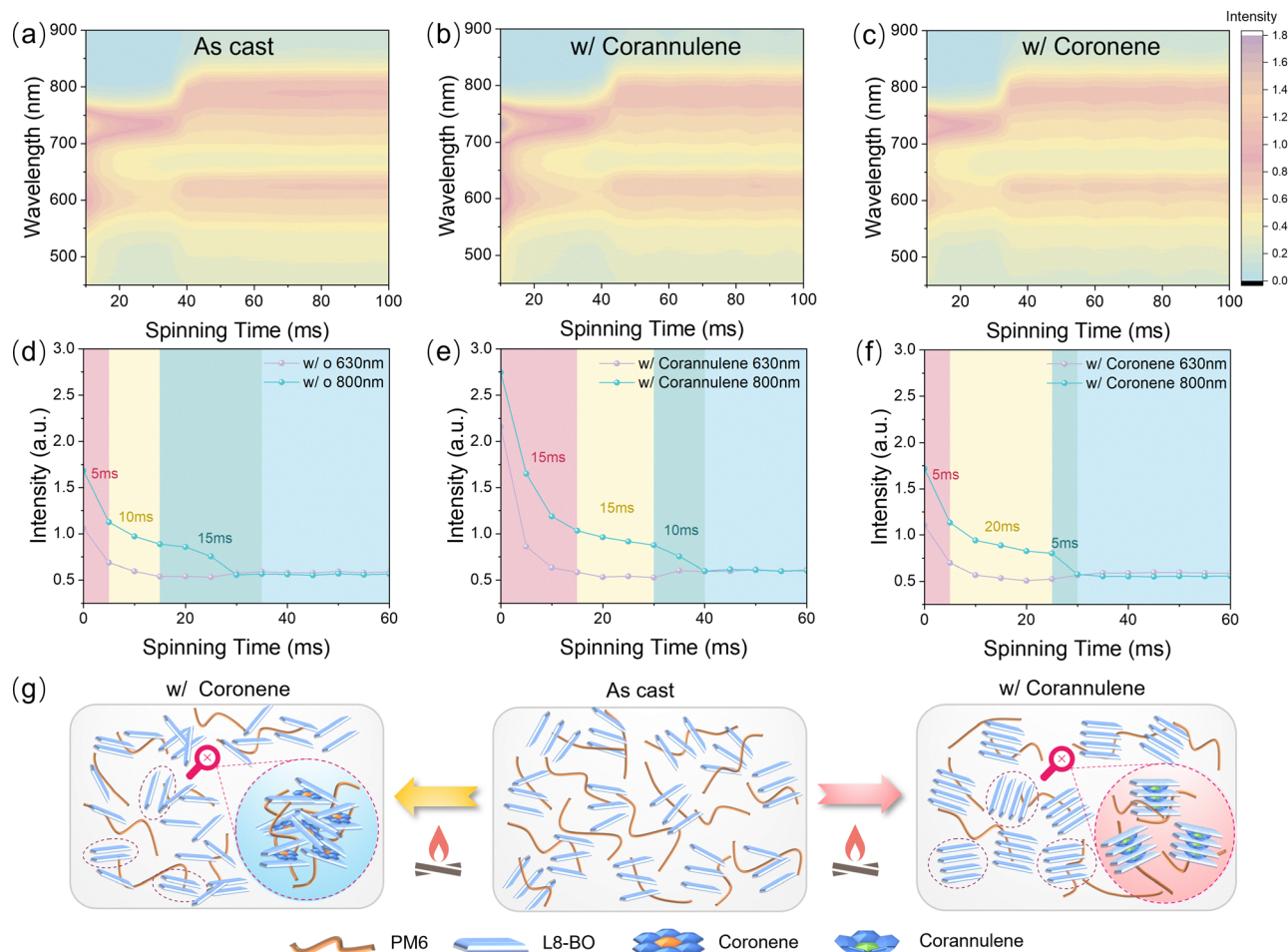


Fig. 7 *In situ* UV-vis absorption color maps and peak intensities of (a) and (d) pristine PM6:L8-BO, (b) and (e) PM6:L8-BO treated with corannulene and (c) and (f) PM6:L8-BO treated with coronene. (g) Schematic illustration showing the effects of planar coronene and bowl-shaped corannulene additives on the blend film microstructure.

III (10 ms) and promoted enhanced film crystallinity. Conversely, the coronene-treated films induced an excessively brief aggregation period (5 ms), resulting in non-uniform phase separation and suboptimal molecular packing, as corroborated by the film morphology results.

Furthermore, the non-volatile solid additives further interact with donor–acceptor materials during annealing, facilitating the optimization of film morphology. As shown in Fig. S21 (ESI[†]), devices treated with corannulene exhibit a prolonged aggregation process during annealing compared to the as-cast film, facilitating improved molecular packing and phase separation. The extended aggregation period allows for better molecular alignment, enhancing the crystallinity and boosting overall device performance. In contrast, devices treated with coronene show a shortened aggregation process, leading to uneven phase separation and suboptimal molecular packing. The reduced aggregation time hampers the optimal organization of the donor–acceptor blend, resulting in poor film morphology and diminished performance. Fig. 7g elucidates the thin-film evolution mechanism of the additive-assisted active layers, revealing their distinct roles in acceptor aggregation. Corannulene prolongs the solvent evaporation, fostering phase separation while refining intermolecular interactions and crystallization, thereby enabling precise aggregation control. This balanced pre-aggregation and aggregation process facilitates optimized phase separation and molecular packing, ultimately contributing to high-performance OSCs. In contrast, the excessively rapid aggregation induced by coronene leads to highly compact molecular π – π stacking, which may negatively impact charge transport and crystallinity, thus hindering performance enhancement.

Conclusion

In summary, we have pioneered the investigation of the impact of two aromatic solid additives with distinct structural curvatures, *i.e.* corannulene and coronene, on the blend film morphology and device performance of OSCs. Our comprehensive theoretical and experimental analyses elucidate how intermolecular interactions between the additives and active layer materials influence the device behavior. The bowl-shaped corannulene, with its higher dipole moment and weaker π – π interactions, exhibits dominant C–H $\cdots\pi$ interactions with the active layer materials, preventing excessive self-aggregation while effectively promoting a more favorable molecular packing of acceptor molecules, significantly enhancing charge transport and exciton dissociation. The unique combination of these characteristics results in significant improvements in charge transport and exciton dissociation. In contrast, the incorporation of coronene disrupted π – π stacking and induced excessive aggregation, which negatively impacted the blend morphology and reduced device efficiency. Notably, introducing corannulene into the PM6:L8-BO blend led to a remarkable PCE of up to 20.52%, ranked as one of the highest values reported for OSCs to date. Furthermore, the corannulene-treated devices exhibited a superior thermal stability with a T_{85} lifetime of 2007 h, significantly outperforming the 52-h lifespan of the as-cast

devices. These findings underscore the great potential of curved solid additives in optimizing OSC molecular packing and morphology, offering innovative pathways for designing highly efficient and long-lifetime OSCs, and setting new benchmarks for future solar cell technologies.

Author contributions

Dr B. Liu, Dr M. An, and Prof. X. Guo conceived the idea. Z. Zhong, Dr B. Liu, and Dr M. An synthesized the additives, fabricated the devices, and conducted the characterizations. Dr S. Gámez-Valenzuela performed the DFT calculations. Dr J.-W. Lee and Prof. B. J. Kim carried out the GIWAXS measurements and analysis. Y. Wang, G. Zhang and Q. Lian measured the energy loss. G. Xie and Prof. L. Qiu performed *in situ* UV-vis absorption characterization. B. Li, W. Zhou, and H. Cai conducted the XPS measurements. Dr D. Hu, C. Xu and Dr Y. Wang performed the TAS measurements. Z. Zhong drafted the manuscript. Dr B. Liu, Dr S. Gámez-Valenzuela, Dr M. An and Prof. X. Guo revised the paper. All authors discussed and commented on the key scientific issues of this work.

Conflicts of interest

The authors declare no competing financial interest.

Data availability

The data that support the findings of this study are available from the corresponding authors upon reasonable request.

Acknowledgements

X. G. acknowledges financial support from the Shenzhen Science and Technology Innovation Bureau (KCXST20221021111413031). B. L. is grateful to the Shenzhen Science and Technology Innovation Bureau (JCYJ20220530113802005) for the financial support. This work was supported by the National Research Foundation of Korea (RS-2024-00432362). The authors are also grateful for the technical support from SUSTech Core Research Facilities and the Computational Science and Engineering of Southern University of Science and Technology.

References

- 1 P. Cheng and X. Zhan, *Chem. Soc. Rev.*, 2016, **45**, 2544–2582.
- 2 H. Li, Y. Li, X. Dai, X. Xu and Q. Peng, *Angew. Chem., Int. Ed.*, 2024, **64**, e202416866.
- 3 J. Song, C. Li, H. Ma, B. Han, Q. Wang, X. Wang, D. Wei, L. Bu, R. Yang, H. Yan and Y. Sun, *Adv. Mater.*, 2024, **36**, 2406922.
- 4 S. Guan, Y. Li, C. Xu, N. Yin, C. Xu, C. Wang, M. Wang, Y. Xu, Q. Chen, D. Wang, L. Zuo and H. Chen, *Adv. Mater.*, 2024, **36**, 2400342.

- 5 H. Chen, W. Sun, R. Zhang, Y. Huang, B. Zhang, G. Zeng, J. Ding, W. Chen, F. Gao, Y. Li and Y. Li, *Adv. Mater.*, 2024, **36**, 2402350.
- 6 G. Li, F. Qin, R. M. Jacobberger, S. Mukherjee, L. O. Jones, R. M. Young, R. M. Pankow, B. P. Kerwin, L. Q. Flagg, D. Zheng, L.-W. Feng, K. L. Kohlstedt, V. K. Sangwan, M. C. Hersam, G. C. Schatz, D. M. DeLongchamp, M. R. Wasielewski, Y. Zhou, A. Facchetti and T. J. Marks, *Joule*, 2023, **7**, 2152–2173.
- 7 H. Chen, Y. Huang, R. Zhang, H. Mou, J. Ding, J. Zhou, Z. Wang, H. Li, W. Chen, J. Zhu, Q. Cheng, H. Gu, X. Wu, T. Zhang, Y. Wang, H. Zhu, Z. Xie, F. Gao, Y. Li and Y. Li, *Nat. Mater.*, 2025, **24**, 444–453.
- 8 C. Lin, R. Peng, W. Song, J. Gao, T. Feng, Y. Bai, Q. Liu, M. Yang, J. Zhang and Z. Ge, *Angew. Chem., Int. Ed.*, 2024, **64**, e202420121.
- 9 S. Wang, S. Wang, J. Wang, N. Yu, J. Qiao, X. Xie, C. Li, M. S. Abbasi, R. Ding, X. Zhang, Y. Han, G. Lu, J. Zhang, X. Hao, Z. Tang, Y. Cai and H. Huang, *Adv. Energy Mater.*, 2025, DOI: [10.1002/aenm.202405205](https://doi.org/10.1002/aenm.202405205).
- 10 C. Li, X. Gu, Z. Chen, X. Han, N. Yu, Y. Wei, J. Gao, H. Chen, M. Zhang, A. Wang, J. Zhang, Z. Wei, Q. Peng, Z. Tang, X. Hao, X. Zhang and H. Huang, *J. Am. Chem. Soc.*, 2022, **144**, 14731–14739.
- 11 L. Zhu, M. Zhang, G. Zhou, Z. Wang, W. Zhong, J. Zhuang, Z. Zhou, X. Gao, L. Kan, B. Hao, F. Han, R. Zeng, X. Xue, S. Xu, H. Jing, B. Xiao, H. Zhu, Y. Zhang and F. Liu, *Joule*, 2024, **8**, 3153–3168.
- 12 Z. Luo, W. Wei, R. Ma, G. Ran, M. H. Jee, Z. Chen, Y. Li, W. Zhang, H. Y. Woo and C. Yang, *Adv. Mater.*, 2024, **36**, 2407517.
- 13 N. Wei, J. Chen, Y. Cheng, Z. Bian, W. Liu, H. Song, Y. Guo, W. Zhang, Y. Liu, H. Lu, J. Zhou and Z. Bo, *Adv. Mater.*, 2024, **36**, 2408934.
- 14 J. Wang, P. Wang, T. Chen, W. Zhao, J. Wang, B. Lan, W. Feng, H. Liu, Y. Liu, X. Wan, G. Long, B. Kan and Y. Chen, *Angew. Chem., Int. Ed.*, 2024, **64**, e202423562.
- 15 J. Fu, Q. Yang, P. Huang, S. Chung, K. Cho, Z. Kan, H. Liu, X. Lu, Y. Lang, H. Lai, F. He, P. W. K. Fong, S. Lu, Y. Yang, Z. Xiao and G. Li, *Nat. Commun.*, 2024, **15**, 1830.
- 16 C. Chen, L. Wang, W. Xia, K. Qiu, C. Guo, Z. Gan, J. Zhou, Y. Sun, D. Liu, W. Li and T. Wang, *Nat. Commun.*, 2024, **15**, 6865.
- 17 Y. Jiang, S. Sun, R. Xu, F. Liu, X. Miao, G. Ran, K. Liu, Y. Yi, W. Zhang and X. Zhu, *Nat. Energy*, 2024, **9**, 975–986.
- 18 Y. Sun, L. Wang, C. Guo, J. Xiao, C. Liu, C. Chen, W. Xia, Z. Gan, J. Cheng, J. Zhou, Z. Chen, J. Zhou, D. Liu, T. Wang and W. Li, *J. Am. Chem. Soc.*, 2024, **146**, 12011–12019.
- 19 F. Zhao, C. Wang and X. Zhan, *Adv. Energy Mater.*, 2018, **8**, 1703147.
- 20 Y. Wang, S. Zhang, J. Wang, J. Ren, J. Qiao, Z. Chen, Y. Yu, X.-T. Hao and J. Hou, *ACS Energy Lett.*, 2024, **9**, 2420–2427.
- 21 S. Lai, Y. Cui, Z. Chen, X. Xia, P. Zhu, S. Shan, L. Hu, X. Lu, H. Zhu, X. Liao and Y. Chen, *Adv. Mater.*, 2024, **36**, 2313105.
- 22 J. Zhang, Z. Li, X. Jiang, L. Xie, G. Pan, A. Buyan-Arivjikh, T. Baier, S. Tu, L. Li, M. Schwartzkopf, S. K. Vayalil, S. V. Roth, Z. Ge and P. Müller-Buschbaum, *Adv. Energy Mater.*, 2025, **15**, 2404724.
- 23 X. Cui, Y. Ji, Y. Liu, X. Ma, H. Li, P. Cheng, W. Huang and Z. Bo, *Adv. Energy Mater.*, 2025, **15**, 2403077.
- 24 K. Shi, J. Lai, X. Xia, S. Jeong, C. Zhu, L. Zhou, J. Guo, J. Zhang, C. Yang, X. Li, L. Meng, Z. Zhang, B. Qiu and Y. Li, *Adv. Funct. Mater.*, 2024, **35**, 2411787.
- 25 W. Su, X. Zhou, Z. Yao, H. Bai, Y. Duan, R. Sun, Y. Wu, Q. Wu, H. Qin, C. Zhao, W. Zhu, H. Y. Woo, J. Min, Y. Li, W. Ma and Q. Fan, *Adv. Funct. Mater.*, 2024, **34**, 2313744.
- 26 Y. Wang, K. Sun, C. Li, C. Zhao, C. Gao, L. Zhu, Q. Bai, C. Xie, P. You, J. Lv, X. Sun, H. Hu, Z. Wang, H. Hu, Z. Tang, B. He, M. Qiu, S. Li and G. Zhang, *Adv. Mater.*, 2024, **36**, 2411957.
- 27 X. He, Z. Liu, H. Chen and C. Li, *Adv. Mater.*, 2024, **36**, 2306681.
- 28 H. He, X. Li, J. Zhang, Z. Chen, Y. Gong, H. Zhuo, X. Wu, Y. Li, S. Wang, Z. Bi, B. Song, K. Zhou, T. Liang, W. Ma, G. Lu, L. Ye, L. Meng, B. Zhang, Y. Li and Y. Li, *Nat. Commun.*, 2025, **16**, 787.
- 29 R. Zhang, H. Chen, T. Wang, L. Kobera, L. He, Y. Huang, J. Ding, B. Zhang, A. Khasbaatar, S. Nanayakkara, J. Zheng, W. Chen, Y. Diao, S. Abbrent, J. Brus, A. H. Coffey, C. Zhu, H. Liu, X. Lu, Q. Jiang, V. Coropceanu, J.-L. Brédas, Y. Li, Y. Li and F. Gao, *Nat. Energy*, 2025, **10**, 124–134.
- 30 C. McDowell, M. Abdelsamie, M. F. Toney and G. C. Bazan, *Adv. Mater.*, 2018, **30**, 1707114.
- 31 H. Ma, J. Song, J. Qiao, B. Han, Q. Wang, M. H. Jee, L. Bu, D. Wei, H. Y. Woo, X. Hao and Y. Sun, *Energy Environ. Sci.*, 2025, **18**, 397–405.
- 32 Y. Wang, W. Sun, Y. Zhang, B. Zhang, Y. Ding, Z. Zhang, L. Meng, K. Huang, W. Ma and H. Zhang, *Angew. Chem., Int. Ed.*, 2024, **64**, e202417643.
- 33 T. Chen, Y. Zhong, T. Duan, X. Tang, W. Zhao, J. Wang, G. Lu, G. Long, J. Zhang, K. Han, X. Wan, B. Kan and Y. Chen, *Angew. Chem., Int. Ed.*, 2025, **64**, e202412983.
- 34 W. Su, X. Zhou, Q. Wu, Y. Wu, H. Qin, Z. Liang, H. Li, H. Bai, J. Guo, L. Jiang, Y. Liu, R. Ma, Y. Li, W. Zhu and Q. Fan, *Adv. Funct. Mater.*, 2024, **35**, 2415090.
- 35 Z. Chen, H. Yao, J. Wang, J. Zhang, T. Zhang, Z. Li, J. Qiao, S. Xiu, X. Hao and J. Hou, *Energy Environ. Sci.*, 2023, **16**, 2637–2645.
- 36 B. Liu, W. Xu, R. Ma, J. Lee, T. A. Dela Peña, W. Yang, B. Li, M. Li, J. Wu, Y. Wang, C. Zhang, J. Yang, J. Wang, S. Ning, Z. Wang, J. Li, H. Wang, G. Li, B. J. Kim, L. Niu, X. Guo and H. Sun, *Adv. Mater.*, 2023, **35**, 2308334.
- 37 Y. Ran, C. Liang, Z. Xu, W. Jing, X. Xu, Y. Duan, R. Li, L. Yu and Q. Peng, *Adv. Funct. Mater.*, 2024, **34**, 2311512.
- 38 J. Wang, Y. Wang, P. Bi, Z. Chen, J. Qiao, J. Li, W. Wang, Z. Zheng, S. Zhang, X. Hao and J. Hou, *Adv. Mater.*, 2023, **35**, 2301583.
- 39 P. Cheng, C. Yan, T. Lau, J. Mai, X. Lu and X. Zhan, *Adv. Mater.*, 2016, **28**, 5822–5829.
- 40 R. Yu, R. Shi, Z. He, T. Zhang, S. Li, Q. Lv, S. Sha, C. Yang, J. Hou and Z. Tan, *Angew. Chem.*, 2023, **135**, e202308367.
- 41 D. Xia, Z. Zhang, C. Zhao, J. Wang, J. Xia, G. Chen, S. Li, Z. Tang, S. You and W. Li, *J. Colloid Interface Sci.*, 2021, **601**, 70–77.

- 42 M.-W. An, B.-S. Wu, S. Wang, Z.-C. Chen, Y. Su, L.-L. Deng, S.-H. Li, Z.-A. Nan, H.-R. Tian, X.-L. Liu, D.-Q. Yun, Q. Zhang, S.-Y. Xie and L.-S. Zheng, *Cell Rep. Phys. Sci.*, 2021, **2**, 100662.
- 43 Z. Xing, M.-W. An, Z.-C. Chen, M. Hu, X. Huang, L.-L. Deng, Q. Zhang, X. Guo, S.-Y. Xie and S. Yang, *J. Am. Chem. Soc.*, 2022, **144**, 13839–13850.
- 44 Z. Xing, F. Liu, S. Li, X. Huang, A. Fan, Q. Huang and S. Yang, *Angew. Chem., Int. Ed.*, 2023, **62**, e202305357.
- 45 E. Nestoros and M. C. Stuparu, *Chem. Commun.*, 2018, **54**, 6503–6519.
- 46 X. Zhang, L. Wang, W. Zhang, Z. Chen, C. Yang, S. Xu, P. Du, B. Chen, Q. He, H. Tian, X. Zhu, M. Li, S. Wang, L. Deng, S. Chen, Q. Zhang, S. Xie and L. Zheng, *Angew. Chem., Int. Ed.*, 2025, **64**, e202413582.
- 47 L. Liu, Y. Kan, K. Gao, J. Wang, M. Zhao, H. Chen, C. Zhao, T. Jiu, A.-Y. Jen and Y. Li, *Adv. Mater.*, 2020, **32**, 1907604.
- 48 A. M. Butterfield, B. Gilomen and J. S. Siegel, *Org. Process Res. Dev.*, 2012, **16**, 664–676.
- 49 X. Song, K. Zhang, R. Guo, K. Sun, Z. Zhou, S. Huang, L. Huber, M. Reus, J. Zhou, M. Schwartzkopf, S. V. Roth, W. Liu, Y. Liu, W. Zhu and P. Müller-Buschbaum, *Adv. Mater.*, 2022, **34**, 2200907.
- 50 X. Zhu, Y. Zhang, B. Xie, J. Miao, W. Ma, J. Liu and L. Wang, *J. Mater. Chem. C*, 2023, **11**, 2144–2152.
- 51 S. Luo, C. Li, J. Zhang, X. Zou, H. Zhao, K. Ding, H. Huang, J. Song, J. Yi, H. Yu, K. S. Wong, G. Zhang, H. Ade, W. Ma, H. Hu, Y. Sun and H. Yan, *Nat. Commun.*, 2023, **14**, 6964.
- 52 D. Zhang, Y. Li, M. Li, W. Zhong, T. Heumüller, N. Li, L. Ying, C. J. Brabec and F. Huang, *Adv. Funct. Mater.*, 2022, **32**, 2205338.
- 53 Y. Miao, Y. Sun, W. Zou, X. Zhang, Y. Kan, W. Zhang, X. Jiang, X. Wang, R. Yang, X. Hao, L. Geng, H. Xu and K. Gao, *Adv. Mater.*, 2024, **36**, 2406623.
- 54 Y. Li, J. Yu, Y. Zhou and Z. Li, *Chem. – Eur. J.*, 2022, **28**, e202201675.
- 55 J. Zhang and M. Dolg, *Phys. Chem. Chem. Phys.*, 2016, **18**, 3003–3010.
- 56 D. Li, N. Deng, Y. Fu, C. Guo, B. Zhou, L. Wang, J. Zhou, D. Liu, W. Li, K. Wang, Y. Sun and T. Wang, *Adv. Mater.*, 2023, **35**, 2208211.
- 57 R. Yu, R. Shi, Z. He, T. Zhang, S. Li, Q. Lv, S. Sha, C. Yang, J. Hou and Z. Tan, *Angew. Chem.*, 2023, **135**, e202308367.
- 58 B. Liu, S. Gámez-Valenzuela, J.-W. Lee, B. Li, W. Yang, K. Wang, Z. Zhong, J. Yang, Z. Wang, C. Xu, H. Sun, B. J. Kim and X. Guo, *ACS Energy Lett.*, 2024, **9**, 3727–3736.
- 59 M. C. Stuparu, *Acc. Chem. Res.*, 2021, **54**, 2858–2870.
- 60 Q. Li, X. Liao, Y. Sun, Y. Xu, S. Liu, L. Wang, Z. Cao, X. Zhan, T. Zhu, B. Xiao, Y. Cai and F. Huang, *Small*, 2024, **20**, 2308165.
- 61 N. B. Kolhe, S. M. West, D. K. Tran, X. Ding, D. Kuzuhara, N. Yoshimoto, T. Koganezawa and S. A. Jenekhe, *Chem. Mater.*, 2020, **32**, 195–204.
- 62 H. Chen, Y. Huang, R. Zhang, H. Mou, J. Ding, J. Zhou, Z. Wang, H. Li, W. Chen, J. Zhu, Q. Cheng, H. Gu, X. Wu, T. Zhang, Y. Wang, H. Zhu, Z. Xie, F. Gao, Y. Li and Y. Li, *Nat. Mater.*, 2025, **24**, 444–453.
- 63 Z. Chen, S. Zhang, T. Zhang, J. Dai, Y. Yu, H. Li, X. Hao and J. Hou, *Joule*, 2024, **8**, 1723–1734.
- 64 R. K. Patel, S. Jonnalagadda and P. K. Gupta, *Pharm. Res.*, 2022, **39**, 1001–1017.
- 65 L. Kong, Z. Zhang, N. Zhao, Z. Cai, J. Zhang, M. Luo, X. Wang, M. Chen, W. Zhang, L. Zhang, Z. Wei and J. Chen, *Adv. Energy Mater.*, 2023, **13**, 2300763.
- 66 R. Xu, Y. Jiang, F. Liu, G. Ran, K. Liu, W. Zhang and X. Zhu, *Adv. Mater.*, 2024, **36**, 2312101.
- 67 L. Kong, Z. Zhang, N. Zhao, Z. Cai, J. Zhang, M. Luo, X. Wang, M. Chen, W. Zhang, L. Zhang, Z. Wei and J. Chen, *Adv. Energy Mater.*, 2023, **13**, 2300763.
- 68 W. Zou, Y. Sun, L. Sun, X. Wang, C. Gao, D. Jiang, J. Yu, G. Zhang, H. Yin, R. Yang, H. Zhu, H. Chen and K. Gao, *Adv. Mater.*, 2025, **37**, 2413125.
- 69 D. Credgington and J. R. Durrant, *J. Phys. Chem. Lett.*, 2012, **3**, 1465–1478.
- 70 J. Zhou, L. Wang, C. Liu, C. Guo, C. Chen, Y. Sun, Y. Yang, J. Cheng, Z. Gan, Z. Chen, W. Sun, J. Zhou, W. Xia, D. Liu, W. Li and T. Wang, *J. Am. Chem. Soc.*, 2024, **146**, 34998–35006.
- 71 T. Jia, T. Lin, Y. Yang, L. Wu, H. Cai, Z. Zhang, K. Lin, Y. Hai, Y. Luo, R. Ma, Y. Li, T. A. Dela Peña, S. Liu, J. Zhang, C. Liu, J. Chen, J. Wu, S. Liu and F. Huang, *Nat. Commun.*, 2025, **16**, 871.
- 72 Y. Ouyang, R. Wang, X. Wang, M. Xiao and C. Zhang, *Sci. Adv.*, 2025, **11**, eadr5973.
- 73 K. Liu, Y. Jiang, F. Liu, G. Ran, M. Wang, W. Wang, W. Zhang, Z. Wei, J. Hou and X. Zhu, *Adv. Mater.*, 2024, **37**, 2413376.
- 74 X. Wu, B. Xiao, R. Sun, X. Yang, M. Zhang, Y. Gao, B. Xiao, E. D. Papkovskaya, Y. Luponosov, C. J. Brabec and J. Min, *Energy Environ. Sci.*, 2025, **18**, 1812–1823.
- 75 T. Dai, Y. Meng, Z. Wang, J. Lu, Z. Zheng, M. Du, Q. Guo and E. Zhou, *J. Am. Chem. Soc.*, 2025, **147**, 4631–4642.
- 76 L. Zhu, M. Zhang, J. Xu, C. Li, J. Yan, G. Zhou, W. Zhong, T. Hao, J. Song, X. Xue, Z. Zhou, R. Zeng, H. Zhu, C.-C. Chen, R. C. I. MacKenzie, Y. Zou, J. Nelson, Y. Zhang, Y. Sun and F. Liu, *Nat. Mater.*, 2022, **21**, 656–663.
- 77 Y. Wei, X. Zhou, Y. Cai, Y. Li, S. Wang, Z. Fu, R. Sun, N. Yu, C. Li, K. Huang, Z. Bi, X. Zhang, Y. Zhou, X. Hao, J. Min, Z. Tang, W. Ma, Y. Sun and H. Huang, *Adv. Mater.*, 2024, **36**, 2403294.
- 78 Y. Cho, Z. Sun, G. Li, D. Zhang, S. Yang, T. J. Marks, C. Yang and A. Facchetti, *J. Am. Chem. Soc.*, 2025, **147**, 758–769.
- 79 J. Zhou, L. Wang, C. Liu, C. Guo, C. Chen, Y. Sun, Y. Yang, J. Cheng, Z. Gan, Z. Chen, W. Sun, J. Zhou, W. Xia, D. Liu, W. Li and T. Wang, *J. Am. Chem. Soc.*, 2024, **146**, 34998–35006.
- 80 Q. Liang, H. Li, W. Xu, J. Lu, R. Ma, Q. Bai, X. Sun, M. Chen, L. Zhu, Q. Liu, Y. Guo, G. Zhang, Q. Xue, A. Iwan, P. Cheng, H. Hu, H. Wang, J. Chen, L. Niu and H. Sun, *Angew. Chem., Int. Ed.*, 2025, **64**, e202425267.
- 81 Z. Xia, C. Gao, Z. Xie, M. Wu, H. Chen, T. Li, J. Zhou, T. Cai, H. Hu, J. Shuai, C. Xie, G. Zhang, W. Chen and S. Liu, *Angew. Chem., Int. Ed.*, 2025, **64**, e202421953.